

## Article

# Corrosion Behavior in Hydrochloric Acid of Pure Titanium after Ultrasonic Severe Surface Rolling

Qisheng Sun<sup>1</sup>, Jiapeng Sun<sup>1,\*</sup> , Jing Han<sup>2</sup> and Guosong Wu<sup>1,\*</sup><sup>1</sup> College of Mechanics and Materials, Hohai University, Nanjing 211100, China<sup>2</sup> Mechanical and Electrical Engineering, China University of Mining and Technology, Xuzhou 221116, China

\* Correspondence: sunpengp@hhu.edu.cn (J.S.); wuguosong@hhu.edu.cn (G.W.)

**Abstract:** Designing a gradient nanostructure is regarded as an effective strategy for strengthening commercial pure Ti without seriously sacrificing ductility. However, the corrosion behavior of the gradient nanostructured (GNS) pure Ti is far from clear, especially in reducing acid in which pure Ti shows poor corrosion resistance. The present paper aims at investigating the corrosion behavior of GNS pure Ti in hydrochloric acid by electrochemical method. The GNS surface layer is produced by a recently developed method called ultrasonic severe surface rolling. The GNS pure Ti exhibits spontaneous passivation behavior as well as the coarse-grained one in 1 M HCl. Due to the GNS surface layer, the corrosion current density and passive current density decrease by 70% and 54%, respectively, giving rise to significantly enhanced corrosion resistance and passivation ability. The better corrosion resistance is believed to be ascribed to the high-density grain boundaries and dislocations induced by the surface nano-grained structure as well as the smooth surface with few surface defects. The USSR processing also enlarges the static water contact angle of the pure Ti to  $61.0 \pm 0.3^\circ$ .

**Keywords:** pure titanium; gradient nanostructure; corrosion; polarization

**Citation:** Sun, Q.; Sun, J.; Han, J.; Wu, G. Corrosion Behavior in Hydrochloric Acid of Pure Titanium after Ultrasonic Severe Surface Rolling. *Metals* **2022**, *12*, 1951. <https://doi.org/10.3390/met12111951>

Academic Editor: Frank Czerwinski

Received: 4 October 2022

Accepted: 11 November 2022

Published: 15 November 2022

**Publisher's Note:** MDPI stays neutral with regard to jurisdictional claims in published maps and institutional affiliations.



**Copyright:** © 2022 by the authors. Licensee MDPI, Basel, Switzerland. This article is an open access article distributed under the terms and conditions of the Creative Commons Attribution (CC BY) license (<https://creativecommons.org/licenses/by/4.0/>).

## 1. Introduction

Commercial pure titanium (Ti) possesses great advantages in terms of low density, high specific strength, excellent corrosion resistance, good biocompatibility, and high formability, and thus is widely applied in marine equipment and engineering, aerospace, rail traffic, 3C products, and biomedicine industry. However, the strength of pure Ti is much lower than its alloys. Although pure Ti exhibits excellent anti-corrosion properties in most environments due to the stable oxidation film covering the surface, its corrosion resistance in some extreme environments is still insufficient, such as in reducing acid. Due to the lack of alloying elements, the available approaches to enhance the corrosion resistance of pure Ti are limited, including regulating microstructure [1,2], using corrosion inhibitors [3,4], and preparing anti-corrosion film [5]. Developing an ingenious microstructure can synchronously improve the strength and corrosion resistance of commercial pure Ti and thus has attracted extensive research attention for expanding its industrial applications.

Preparing the gradient nanostructure has been proven to be an effective strategy for strengthening metallic materials without seriously sacrificing their ductility [6–11]. The introduction of the gradient nanostructure can also greatly enhance fatigue properties. In the past two decades, this strategy has also applied to pure Ti and Ti alloys [12–20]. For example, Huang et al. [21] prepared a gradient nanostructured (GNS) pure Ti through deep rolling treatment, thus significantly improving strength compared to its coarse-grained (CG) counterparts. The authors also investigated the thermal stability of the resulting gradient nanostructure. Lei et al. [22] obtained a high strength-plasticity synergy in the pure Ti by introducing the gradient nanostructure by ultrasonic surface rolling. Li et al. [23] found that the GNS pure Ti prepared by ultrasonic surface rolling was more resistant to high-cycle fatigue than its coarse-grained counterparts.

However, little attention has been paid to the corrosion behavior of the GNS pure Ti. Fu et al. [24,25] reported that the surface mechanical attrition treatment (SMAT) promoted a more stable passive film on the surface of pure Ti in NaCl solution, thus decreasing the corrosion current density. The used SMAT is a general method of preparing the gradient nanostructure [26]. Lu et al. [27] prepared a GNS pure Ti by sliding friction treatment and investigated the in vitro corrosion behavior and biocompatibility. Their result indicated that the GNS pure Ti exhibits an improved corrosion resistance in simulated body fluid solution due to the formation of a thick passive film. These studies all demonstrate that a high density of grain boundaries in the nano-grained surface of the GNS pure Ti is beneficial to the formation of a more protective passive film, thus enhancing corrosion resistance. It is necessary to further reveal the corrosion behavior of the GNS pure Ti in more corrosive environments to deepen the understanding of its corrosion mechanism and expand its applications.

The surface microstructure and surface quality have a large impact on the corrosion resistance of the GNS metals. Most of the methods of preparing GNS metals induce surface defects, contaminations, and large surface roughness, giving rise to degraded surface quality [28–30]. This is generally harmful to surface-sensitive properties, such as corrosion resistance. Balusamy et al. [28] found that SMAT increased the surface roughness of AISI 409 stainless steel, and the resultant surface roughness strongly depended on the processing parameters. The overlarge surface roughness led to decreased corrosion resistance, while the GNS sample with a small increment in surface roughness exhibited improved corrosion resistance. To eliminate the deleterious effect of the degraded surface roughness, post-processing, such as mechanical grinding and polishing, is commonly used to improve the surface quality of the GNS metals [31], which increases the complexity of the process.

Developing a new fabrication process to effectively produce a GNS surface layer with a high-quality surface is still an essential task in the field of gradient nanostructured metallic materials. Recently, a new method to prepare the GNS surface layer called ultrasonic severe surface rolling (USSR) was developed by the present authors [32]. USSR has a great advantage in terms of effectively producing a thick GNS surface layer with a high-quality surface and therefore promotes the superior strength-ductility combination in 316L stainless steel, Cu-Zn alloy, pure Ti, and ZE41 Mg alloy [32–36]. The USSR process has also enhanced the corrosion resistance of 316L in NaCl solution and pure Ti in Hank's solution [34,36].

Pure Ti is frequently used in marine equipment and serves in acid rain zones, which introduces an extreme corrosion environment (low pH value and high  $\text{Cl}^-$ ) [37]. To the best of the authors' knowledge, the corrosion behavior of the GNS pure Ti in this environment has not been reported. The present paper aims to investigate the corrosion behavior of the GNS pure Ti in 1 M HCl solution compared to its CG counterparts through electrochemical measurements. The GNS pure Ti is prepared through USSR processing, which synchronously produces a high-quality surface. The GNS surface layer greatly improves the corrosion performance of pure Ti in hydrochloric acid. The associated mechanism of the improved corrosion resistance is discussed. This work deepens our understanding of the corrosion behavior of GNS pure Ti in extreme corrosion environments and provides an approach to enhance the corrosion resistance of commercial pure Ti in an environment with low pH and high  $\text{Cl}^-$ .

## 2. Materials and Methods

### 2.1. Material Preparation

The commercial Grade 2 Ti plate was used in this work, which was provided by BaoTai Group Co., Ltd., Baoji, China, and processed according to the Chinese standard test GB/T 3621-2007. The as-received sample was cut into cubic samples (20 mm × 50 mm × 2 mm) and then ground using SiC sandpaper of #180, #400, and #800 in turn to obtain a smooth surface. The as-received sample is denoted as the CG sample. Subsequently, the as-received samples were processed by USSR for one pass. During USSR processing, a free rolling cemented carbide ball (14 mm in diameter), which was vibrating synchronously by an

ultrasonic device, scanned the sample line by line with a constant velocity of 0.01 m/s, a feed interval of 0.1 mm, and a static load of 1000 N. The processing parameters refer to our other studies of Mg alloy and pure Ti [32,36]. The USSR-processed sample is denoted as the GNS sample.

## 2.2. Microstructure Characterization

The cross-sectional microstructure of the GNS sample was characterized by an optical microscope and transmission electron microscope (TEM, FEI, Talos, F200X, Thermo Fisher Scientific Inc., Waltham, MA, USA). The microstructure of the CG sample was characterized by an optical microscope. The optical microscopy observation for both CG and GNS samples was conducted along the cross-section. The specimens were mechanically ground, polished, and then etched using the Kroll solution. The TEM observation of the GNS sample was conducted at the depth of about 20  $\mu\text{m}$  from the USSR-processed surface along the cross-section. Before TEM observation, a 500- $\mu\text{m}$ -thick foil was first machined using a low-speed saw along the longitudinal section. Then, this foil was thinned through mechanical grinding followed by ion milling around the surface on a Gatan 695 ion polishing system (Gatan, Pleasanton, CA, USA).

## 2.3. Electrochemical Measurements and Contact Angle Tests

The potentiodynamic polarization measurements were carried out in 1 M HCl solution on a Gamry 600+ electrochemical workstation using a conventional three-electrode system at room temperature. A platinum foil and saturated calomel electrode (SCE) were used as the counter electrode and reference electrode, respectively. For electrochemical measurements, the CG sample was ground with SiC sandpaper of #180, #400, and #800 in turn, and the GNS sample was slightly polished using ethyl alcohol to remove the surface contaminants. Then, the CG and GNS samples were sealed using silicone rubber with an area of 0.5 cm  $\times$  0.5 cm exposed to hydrochloric acid as the working electrode. Before electrochemical measurements, the samples were immersed in the 1 M HCl solution for 60 min. Then, the potentiodynamic polarization measurements were conducted, for which potential was continuously scanned from  $-0.6$  to  $2 V_{\text{SCE}}$  relative to open circuit potential with a constant rate of 0.33 mV/s. After potentiodynamic polarization measurements, the surface morphologies were observed using scanning electron microscopy on a Hitachi Regulus8100 (Hitachi, Tokyo, Japan). The static water contact angles were measured using a contact angle meter (POWEREACH, JC2000D1). The CG samples for contact angle tests were ground with SiC sandpaper up to #800, and the GNS samples were slightly polished using ethyl alcohol to remove the surface contaminants. All the electrochemical and contact angle tests were independently repeated three times to ensure the reproducibility of the data.

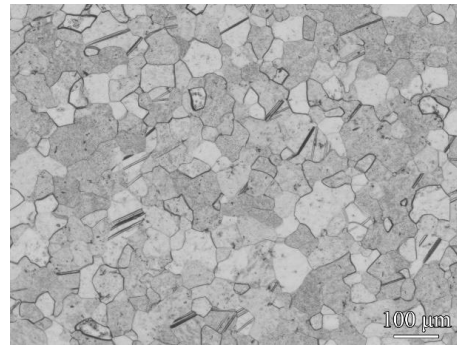
## 3. Results

Figure 1 illustrates one sample piece after USSR processing. The processing region is smooth and without visible cracks and other processing defects, showing a good mirror effect. This smooth surface results from the USSR-induced severe surface plastic deformation.



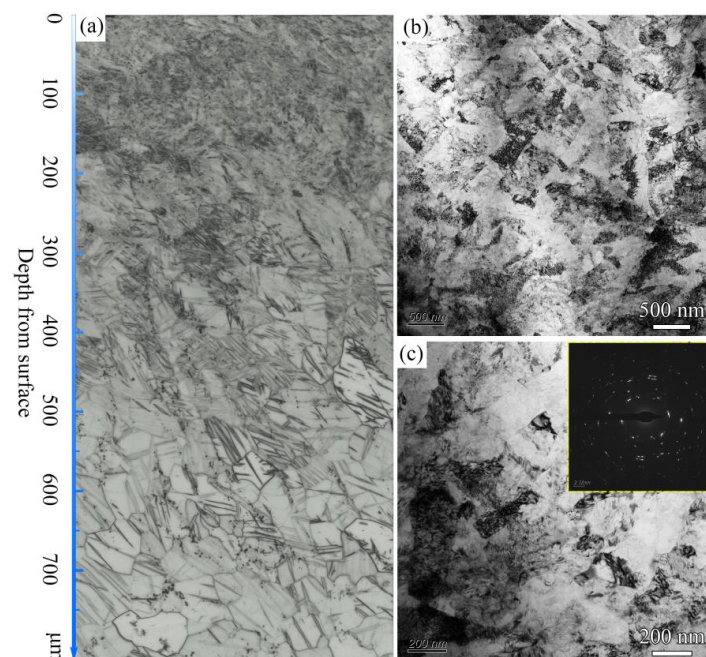
**Figure 1.** Appearance of the sample after USSR processing.

Figure 2 presents the optical micrograph of the CG sample. The microstructure of this sample is featured by homogenous equiaxed grains, giving rise to a recrystallized structure. The mean grain size is approximately  $45\ \mu\text{m}$  measured by the line intercept method, indicating a coarse-grained structure. A few twins are also found in the CG sample.



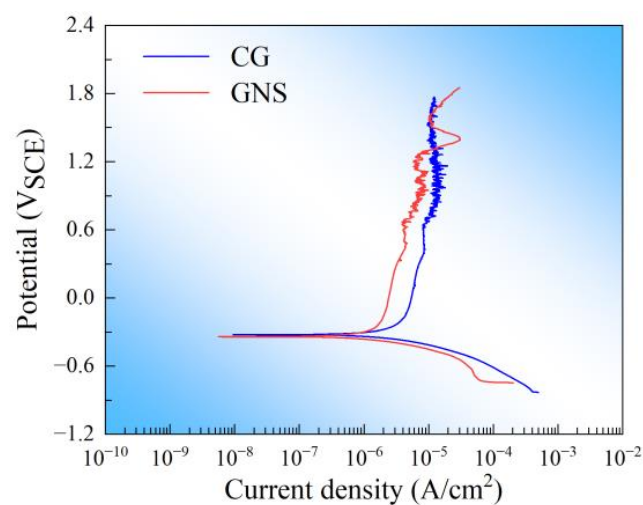
**Figure 2.** Optical micrograph of the CG sample.

Figure 3 depicts the microstructure of the GNS sample along the longitudinal section. At the top  $\sim 400\text{-}\mu\text{m}$ -thick surface layer, the microstructure is remarkably refined, and grain size increases with depth, as shown in Figure 3a. Dense twins are also found at a depth range of 200 to  $1300\ \mu\text{m}$ , and their density is greatly larger than that in the CG sample. Previous studies have proven that the deformation twin is the main deformation mode of pure Ti as well as dislocations [38]. The TEM observation indicates that the microstructure is mainly composed of elongated nanograins with an average thickness of  $172\ \text{nm}$  at the depth of about  $20\ \mu\text{m}$ , as depicted in Figure 3b,c. The high density of dislocations and dislocation tangles are also observed within the nanograins. The selected area electron diffraction (SAED) pattern reveals that these nanograins are surrounded by both high-angle grain boundaries (HAGBs) and low-angle grain boundaries (LAGBs). Our microstructure characterization reveals a GNS surface layer in pure Ti produced by USSR processing.



**Figure 3.** Microstructure of the GNS sample: (a) optical micrograph; (b,c) TEM images at the depth of about  $20\ \mu\text{m}$  from the USSR processed surface. The insert in panel c shows the corresponding SAED pattern.

Figure 4 presents the polarization measurement result of the CG and GNS samples. The corrosion parameters, including corrosion potential  $E_{corr}$ , corrosion current density  $i_{corr}$ , and passive current density  $i_{pass}$ , are extracted from the polarization curves and collected in Table 1. The GS and CG samples exhibit similar polarization curves, giving rise to similar cathodic and anodic reactions. For the anodic branch, both samples immediately enter a steady passivation region and have not shown a pitting phenomenon within the scanning potential range of  $-0.6$  to  $2$   $V_{SCE}$ . This result indicates that both samples exhibit a spontaneous passivation behavior and have a wide passive range and perfect passivation ability in hydrochloric acid. As the potential exceeds  $0.6$   $V_{SCE}$ , current fluctuation is observed for both samples, which is possibly related to the competition between the formation and dissolution of oxide film [39]. A transition current is observed after approximately  $1.3$   $V_{SCE}$ , which is frequently reported in the Ti alloy and may be caused by the oxygen reaction [39,40].



**Figure 4.** Potentiodynamic polarization curves of the CG and GNS samples.

**Table 1.** Corrosion parameters obtained from the polarization curves.

	$E_{corr}$ ( $V_{SCE}$ )	$i_{corr}$ ( $\mu A/cm^2$ )	$i_{pass}$ ( $\mu A/cm^2$ )
CG	$-0.340 \pm 0.012$	$4.25 \pm 0.42$	$8.12 \pm 0.47$
GNS	$-0.342 \pm 0.007$	$1.28 \pm 0.08$	$3.73 \pm 0.71$

The polarization curve of the GNS sample moves towards the left compared to that of the CG sample, giving rise to decreased corrosion current density and passive current density. The current density at a potential of  $0.5$   $V_{SCE}$  is artificially appointed as passive current density. The passive current density of the CG sample ( $8.12 \pm 0.47$   $\mu A/cm^2$ ) is more than two times higher than that of the GNS sample ( $3.73 \pm 0.71$   $\mu A/cm^2$ ). The corrosion current density of the CG sample ( $4.25 \pm 0.42$   $\mu A/cm^2$ ) is more than three times higher than that of the GNS sample ( $1.28 \pm 0.08$   $\mu A/cm^2$ ). Moreover, the two investigated samples have similar corrosion potential, as shown in Table 1. The smaller passive current density generally means the easier generation of passivation behavior, and the smaller corrosion current density means a lower corrosion rate [41–43]. The greatly decreased passive current density and corrosion current density demonstrate that USSR processing significantly improves the protective ability of the passive film and the corrosion resistance of commercial pure Ti in hydrochloric acid.

Figure 5 presents the SEM surface morphologies of the CG and GNS samples. There are no visible pitting corrosion pits for both samples, indicating that pitting corrosion has not activated, which agrees well with the result of the potentiodynamic polarization measurements. Many deep and wide grooves are found in the CG sample because it is

ground using raw sandpaper, while a smooth surface is observed in the GNS sample with some small pits but without other obvious processing defects, such as cracks.

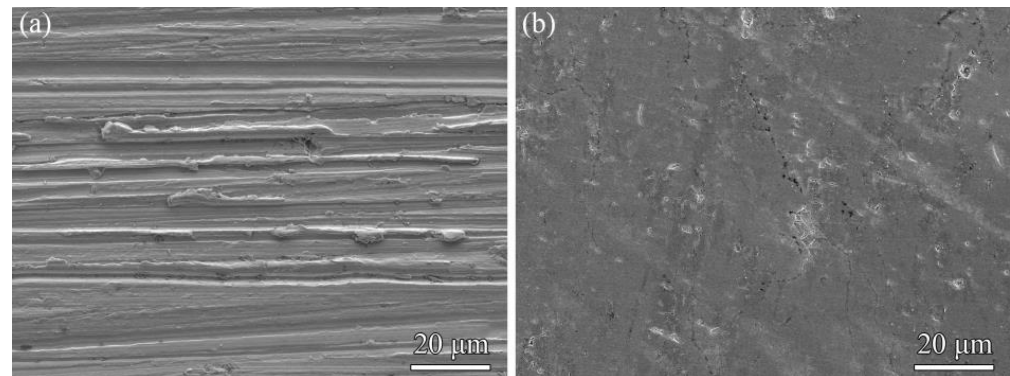


**Figure 5.** Surface morphologies of the (a) CG and (b) GNS samples after polarization.

Figure 6 shows the results of the static water contact angle tests of the CG and GNS samples. The static water contact angle of the pure Ti enlarges from  $48.6 \pm 0.3^\circ$  to  $61.0 \pm 0.3^\circ$  after USSR processing. This result indicates that both the CG sample and the GNS sample have a hydrophilic surface. It is suggested that the variation of the water contact angle is related to the changed surface roughness and surface state induced by USSR.

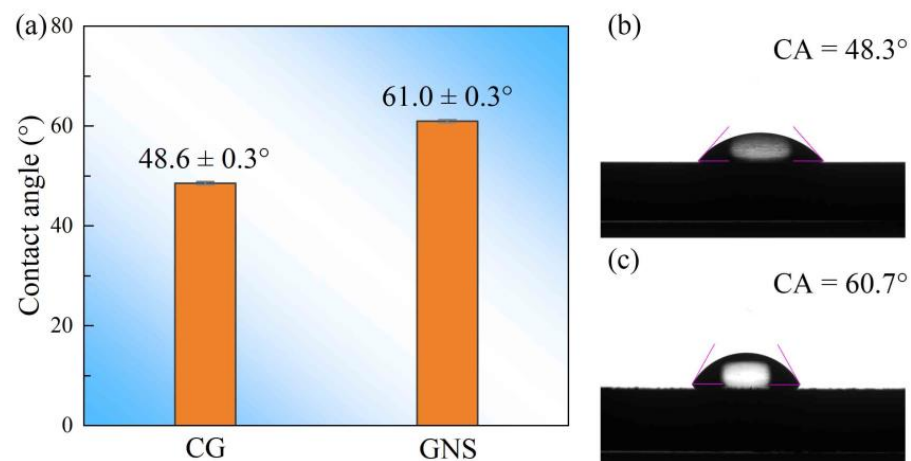


**Figure 6.** (a) Water contact angle. (b) Water droplet on the CG sample. (c) Water droplet on the GNS sample.

#### 4. Discussion

Our study demonstrates a significantly enhanced corrosion resistance of the commercial pure Ti in hydrochloric acid through the introduction of the GNS surface layer prepared by the USSR. The improved corrosion resistance of the pure Ti through introducing surface or bulk nanograins or ultra-fine grains by other techniques is also reported. For example, Balyanov et al. [43] reported that the ultrafine-grained pure Ti exhibited decreased corrosion resistance in hydrochloric acid compared to its CG counterparts, but the difference is only 4.1–4.7% depending on the concentration of the hydrochloric acid. The authors also found that the ultrafine-grained and CG samples had similar passive current densities. Limited improvement in anti-corrosion properties was also found in the GNS pure Ti prepared by SMAT in NaCl solution [24]. Here, the corrosion current density and passive current density of the GNS sample reduce by 70% and 54% compared to the CG sample, giving rise to significantly improved anti-corrosion properties. It is evident that the USSR process has

a great advantage in terms of enhancing the corrosion resistance of pure Ti as compared to other technologies.

Our polarization tests indicate that both GNS and CG samples exhibit a spontaneous passivation behavior, while the GNS sample has a low passive current density. This implies that a stable passive film is formed covering the surface of both samples in hydrochloric acid, and it is more protective for the GNS sample than the CG sample. Zhou et al. [37] reported that the passive film of pure Ti was mainly composed of  $\text{TiO}_2$  in hydrochloric acid. The enhanced passivation ability of the GNS sample must be related to the microstructure evolution, i.e., the formation of a surface nano-grained structure with high-density dislocations. This unique surface microstructure significantly increases the volume fraction of grain boundaries and dislocation density compared to the CG structure. Previous studies have proven that the passive film was preferentially nucleated at lattice defects due to their high activity, such as grain boundaries and dislocations [44]. Therefore, the GNS provides many more nucleation sites for the rapid formation of the passive film, thus promoting better corrosion resistance. Indeed, the rapid formation of the passive film is generally used to explain the enhanced anti-corrosion properties of the nano-grained or ultrafine-grained pure Ti [43,45,46]. Moreover, Lu et al. [27] found that the passive film on the surface of the GNS pure Ti was thicker than that of the CG pure Ti in the simulated body fluid solution. The thickened passive film is generally found in nanocrystalline stainless steel, Ni, and Ti alloy [47]. It is believed that the thickened passive film is related to the massive oxidation channels induced by high-density grain boundaries and other lattice defects [27,47]. Therefore, it is suggested that the surface nano-grained structure in the GNS sample renders a thicker and more compact passive film than the CG sample, thus enhancing the corrosion resistance.

Here, USSR processes a smoother surface accompanied by the formation of the GNS surface layer in pure Ti, giving rise to reduced surface roughness and few surface defects. The reduced surface roughness has been proven to be beneficial to the corrosion resistance of Ti alloy [48]. On the one hand, it is widely assumed that the smooth surface has a high local electron work function (EWF), which means there is difficulty in releasing electrons, resulting in high resistance to corrosion [49]. On the other hand, the smooth surface has a small solid–liquid contact area than the rough surface when it is exposed to a corrosive medium [50,51]. In addition, the smooth surface of the GNS sample is also responsible for the enlarged static water contact angle. Moreover, some studies reported that the gradient nanostructured surface layer could bring out degraded corrosion resistance due to surface defects during processing [28,29]. Here, a mirror surface without obvious surface defects is produced by USSR, thus circumventing the detrimental effect of the surface defects.

## 5. Conclusions

The corrosion behavior of the GNS pure Ti prepared by USSR is investigated in hydrochloric acid. Here, the GNS pure Ti exhibits a spontaneous passivation behavior in 1 M HCl as well as the CG pure Ti. However, the GNS surface layer can significantly improve the corrosion resistance of commercial pure Ti, which is manifested by decreased corrosion current density and reduced passive current density. In our experiment, the corrosion current density decreases from  $4.25 \pm 0.42$  to  $1.28 \pm 0.08 \mu\text{A}/\text{cm}^2$ , and the passive current density decreases from  $8.12 \pm 0.47$  to  $3.73 \pm 0.71 \mu\text{A}/\text{cm}^2$ . The better corrosion resistance of the GNS pure Ti is believed to stem from the high-density grain boundaries and dislocations derived from the surface nano-grained structure, as well as the smooth surface, with few surface defects.

**Author Contributions:** Conceptualization, J.S. and G.W.; methodology, Q.S. and J.H.; investigation, Q.S.; data curation, Q.S.; writing—original draft preparation, Q.S.; writing—review and editing, J.H., J.S. and G.W.; visualization, Q.S.; supervision, J.S. and G.W.; funding acquisition, J.S. and G.W. All authors have read and agreed to the published version of the manuscript.

**Funding:** This research was funded by Fundamental Research Funds for the Central Universities of China, grant number B210202094, and Chinese Jiangsu Specially-appointed Professor Research Grant, grant number HHU 2016B1203507.

**Data Availability Statement:** The data presented in this study are available on request from the corresponding author.

**Conflicts of Interest:** The authors declare no conflict of interest.

## References

1. Nie, M.Y.; Wang, C.T.; Qu, M.H.; Gao, N.; Wharton, J.A.; Langdon, T.G. The corrosion behaviour of commercial purity titanium processed by high-pressure torsion. *J. Mater. Sci.* **2014**, *49*, 2824–2831. [[CrossRef](#)]
2. Sotniczuk, A.; Chrominski, W.; Adamczyk-Cieslak, B.; Pisarek, M.; Garbacz, H. Corrosion behavior of biomedical Ti under simulated inflammation: Exploring the relevance of grain refinement and crystallographic texture. *Corros. Sci.* **2022**, *200*, 110238. [[CrossRef](#)]
3. El Faydy, M.; Galai, M.; Touir, R.; El Assyry, A.; Ebn Touhami, M.; Benali, B.; Lakhrissi, B.; Zarrouk, A. Experimental and theoretical studies for steel XC38 corrosion inhibition in 1 M HCl by N-(8-hydroxyquinolin-5-yl)-methyl)-N-phenylacetamide. *J. Mater. Environ. Sci.* **2016**, *7*, 1406–1416.
4. Errahmany, N.; Rbaa, M.; Abousalem, A.S.; Tazouti, A.; Galai, M.; Kafssaoui, E.H.E.; Touhami, M.E.; Lakhrissi, B.; Touir, R. Experimental, DFT calculations and MC simulations concept of novel quinazolinone derivatives as corrosion inhibitor for mild steel in 1.0 M HCl medium. *J. Mol. Liq.* **2020**, *312*, 113413. [[CrossRef](#)]
5. Zheng, C.Y.; Wen, H.; Etefagh, A.H.; Zhang, B.; Gao, J.; Haghshenas, A.; Rausch, J.R.; Guo, S.M. Laser nitriding of titanium surface for biomedical applications. *Sur. Coat. Technol.* **2020**, *385*, 125397. [[CrossRef](#)]
6. Han, J.; Wang, C.; Song, Y.M.; Liu, Z.Y.; Sun, J.P.; Zhao, J.Y. Simultaneously improving mechanical properties and corrosion resistance of as-cast AZ91 Mg alloy by ultrasonic surface rolling. *Int. J. Min. Met. Mater.* **2022**, *29*, 1551–1558. [[CrossRef](#)]
7. Li, K.J.; Wu, X.; Chen, L.P.; Chen, D.M.; Zhu, G.J.; Shen, Q.; Yoon, J.H. Residual stress and microstructure characterization of 34CrMo4 steel modified by shot peening. *Scanning* **2020**, *2020*, 5367345. [[CrossRef](#)]
8. Li, X.Y.; Lu, L.; Li, J.G.; Zhang, X.; Gao, H.J. Mechanical properties and deformation mechanisms of gradient nanostructured metals and alloys. *Nat. Rev. Mater.* **2020**, *5*, 706–723. [[CrossRef](#)]
9. Chen, L.B.; Cao, T.H.; Wei, R.; Tang, K.; Xin, C.; Jiang, F.; Sun, J. Gradient structure design to strengthen carbon interstitial Fe<sub>40</sub>Mn<sub>40</sub>Co<sub>10</sub>Cr<sub>10</sub> high entropy alloys. *Mater. Sci. Eng. A* **2020**, *772*, 138661. [[CrossRef](#)]
10. Zhang, Q.H.; Li, J.G.; Jiang, K.; Li, P.; Li, Y.S.; Zhang, Y.; Suo, T. Gradient structure induced simultaneous enhancement of strength and ductility in AZ31 mg alloy with twin-twin interactions. *J. Magnes. Alloy.* **2021**, *in press*. [[CrossRef](#)]
11. Li, B.; Niu, C.M.; Zhang, T.L.; Chen, G.Y.; Zhang, G.; Wang, D.; Zhou, X.Y.; Zhu, J.M. Advances of machining techniques for gradient structures in multi-principal-element alloys. *Rare Met.* **2022**, *41*, 4015–4026. [[CrossRef](#)]
12. Liu, Q.; Li, Y.X.; Qiu, J.; Chen, M.A.; Wang, J.; Hu, J. Antibacterial property and bioadaptability of Ti6Al4V alloy with a silvered gradient nanostructured surface layer. *Rare Met.* **2022**, *41*, 621–629. [[CrossRef](#)]
13. Guo, Y.S.; Jia, B.; Zhou, Q.; Liu, R.; Arab, A.; Chen, W.; Ren, Y.P.; Ran, C.; Chen, P.W. Shock induced gradient microstructure with hierarchical nanotwins to enhance mechanical properties of Ti6Al4V alloy. *J. Mater. Process. Technol.* **2022**, *307*, 117693. [[CrossRef](#)]
14. Teng, X.F.; Jia, Y.F.; Gong, C.Y.; Zhang, C.C.; Zhang, X.C.; Tu, S.T. Effect of ultrasonic surface deep rolling combined with oxygen boost diffusion treatment on fatigue properties of pure titanium. *Sci. Rep.* **2021**, *11*, 17840. [[CrossRef](#)]
15. Yan, X.C.; Yin, S.; Chen, C.Y.; Jenkins, R.; Lupoi, R.; Bolot, R.; Ma, W.Y.; Kuang, M.Y.; Kuang, M.; Liao, H.L.; et al. Fatigue strength improvement of selective laser melted Ti6Al4V using ultrasonic surface mechanical attrition. *Mater. Res. Lett.* **2019**, *7*, 327–333. [[CrossRef](#)]
16. Jia, Y.F.; Liu, Y.X.; Huang, J.; Fu, Y.; Zhang, X.C.; Xin, Y.C.; Tu, S.T.; Mao, M.D.; Yang, F.Q. Fatigue-induced evolution of nanograins and residual stress in the nanostructured surface layer of Ti-6Al-4V. *Mater. Sci. Eng. A* **2019**, *764*, 138205. [[CrossRef](#)]
17. Wang, Q.; Ren, J.Q.; Wang, Y.L.; Xin, C.; Xiao, L.; Yang, D. Deformation and fracture mechanisms of gradient nanograined pure Ti produced by a surface rolling treatment. *Mater. Sci. Eng. A* **2019**, *754*, 121–128. [[CrossRef](#)]
18. Ye, Y.D.; Li, X.P.; Sun, Z.Y.; Wang, H.B.; Tang, G.Y. Enhanced surface mechanical properties and microstructure evolution of commercial pure titanium under Electropulsing-Assisted ultrasonic surface rolling process. *Acta Metall. Sin. (Engl. Lett.)* **2018**, *31*, 1272–1280. [[CrossRef](#)]
19. Yin, Y.F.; Xu, W.; Sun, Q.Y.; Xiao, L.; Sun, J. Deformation and fracture behavior of commercial pure Titanium with gradient nano-to-micron-grained surface layer. *Trans. Nonferrous Met. Soc. China* **2015**, *25*, 738–747. [[CrossRef](#)]
20. Jia, Y.F.; Pan, R.J.; Zhang, P.Y.; Sun, Z.T.; Chen, X.R.; Zhang, X.C.; Wu, X.J. Enhanced surface strengthening of titanium treated by combined surface deep-rolling and oxygen boost diffusion technique. *Corros. Sci.* **2019**, *157*, 256–267. [[CrossRef](#)]
21. Huang, J.; Zhang, K.M.; Jia, Y.F.; Zhang, C.C.; Zhang, X.C.; Ma, X.F.; Tu, S.T. Effect of thermal annealing on the microstructure, mechanical properties and residual stress relaxation of pure titanium after deep rolling treatment. *J. Mater. Sci. Technol.* **2019**, *35*, 409–417. [[CrossRef](#)]

22. Lei, L.; Zhao, Q.Y.; Zhao, Y.Q.; Wu, C.; Huang, S.X.; Jia, W.J.; Zeng, W.D. Gradient nanostructure, phase transformation, amorphization and enhanced strength-plasticity synergy of pure titanium manufactured by ultrasonic surface rolling. *J. Mater. Process. Technol.* **2022**, *299*, 117322. [[CrossRef](#)]
23. Li, X.; Sun, B.H.; Guan, B.; Jia, Y.F.; Gong, C.Y.; Zhang, X.C.; Tu, S.T. Elucidating the effect of gradient structure on strengthening mechanisms and fatigue behavior of pure titanium. *Int. J. Fatigue* **2021**, *146*, 106142. [[CrossRef](#)]
24. Fu, T.L.; Zhan, Z.L.; Zhang, L.; Yang, Y.R.; Liu, Z.; Liu, J.X.; Li, L.; Yu, X.H. Effect of surface mechanical attrition treatment on corrosion resistance of commercial pure titanium. *Surf. Coat. Technol.* **2015**, *280*, 129–135. [[CrossRef](#)]
25. Fu, T.L.; Wang, X.; Liu, J.X.; Li, L.; Yu, X.H.; Zhan, Z.L. Characteristics and corrosion behavior of pure titanium subjected to surface mechanical attrition. *JOM* **2017**, *69*, 1844–1847. [[CrossRef](#)]
26. Olugbade, T.O.; Lu, J. Literature review on the mechanical properties of materials after surface mechanical attrition treatment (SMAT). *Nano Mater. Sci.* **2020**, *2*, 3–31. [[CrossRef](#)]
27. Lu, J.W.; Zhang, Y.; Huo, W.T.; Zhang, W.; Zhao, Y.Q.; Zhang, Y.S. Electrochemical corrosion characteristics and biocompatibility of nanostructured titanium for implants. *Appl. Surf. Sci.* **2018**, *434*, 63–72. [[CrossRef](#)]
28. Balusamy, T.; Kumar, S.; Sankara Narayanan, T.S.N. Effect of surface nanocrystallization on the corrosion behaviour of AISI 409 stainless steel. *Corros. Sci.* **2010**, *52*, 3826–3834. [[CrossRef](#)]
29. Hao, Y.W.; Deng, B.; Zhong, C.; Jiang, Y.M.; Li, J. Effect of surface mechanical attrition treatment on corrosion behavior of 316 stainless steel. *J. Iron Steel Res. Int.* **2009**, *16*, 68–72. [[CrossRef](#)]
30. Beura, V.K.; Karanth, Y.; Darling, K.; Solanki, K. Role of gradient nanograined surface layer on corrosion behavior of aluminum 7075 alloy. *NPJ Mater. Degrad.* **2022**, *6*, 62. [[CrossRef](#)]
31. Chen, X.D.; Li, Y.S.; Zhu, Y.T.; Bai, Y.K.; Yang, B. Improved corrosion resistance of 316LN stainless steel performed by rotationally accelerated shot peening. *Appl. Surf. Sci.* **2019**, *481*, 1305–1312. [[CrossRef](#)]
32. Han, J.; Sun, J.P.; Song, Y.M.; Xu, B.Q.; Yang, Z.Q.; Xu, S.S.; Han, Y.; Wu, G.S.; Zhao, J.Y. Achieving gradient heterogeneous structure in Mg alloy for excellent strength-ductility synergy. *J. Magnes. Alloy.* **2022**, *in press*. [[CrossRef](#)]
33. Liu, Y.; Sun, J.P.; Fu, Y.T.; Xu, B.Q.; Li, B.J.; Xu, S.S.; Huang, P.L.; Chen, J.Q.; Han, J.; Wu, G.S. Tuning strength-ductility combination on selective laser melted 316L stainless steel through gradient heterogeneous structure. *Addit. Manuf.* **2021**, *48*, 102373. [[CrossRef](#)]
34. Sun, J.P.; Sun, Q.S.; Liu, Y.; Li, B.J.; Zhang, Z.; Xu, B.Q.; Xu, S.S.; Han, Y.; Qiao, Y.X.; Han, J.; et al. Improving corrosion resistance of selective laser melted 316L stainless steel through ultrasonic severe surface rolling. *J. Mater. Res. Technol.* **2022**, *20*, 4378–4391. [[CrossRef](#)]
35. Sun, Q.S.; Sun, J.P.; Fu, Y.T.; Xu, B.Q.; Han, Y.; Chen, J.Q.; Han, J.; Wu, H.; Wu, G.S. Preparing thick gradient surface layer in Cu-Zn alloy via ultrasonic severe surface rolling for strength-ductility balance. *Materials* **2022**, *15*, 7687. [[CrossRef](#)]
36. Han, J.Z.Z.; Song, Y.M.; Sun, Q.S.; Liu, Z.Y.; Sun, J.P.; Zhao, J.Y. Preparation of gradient nanostructured pure Ti plate with high performance by USSR and its microstructure and properties. *Chin. J. Mech. Eng.* **2022**, *in press*.
37. Zhou, S.F.; Zhao, Y.; Wang, X.J.; Li, W.; Chen, D.C.; Sercombe, T.B. Enhanced corrosion resistance of Ti-5 wt.% TiN composite compared to commercial pure Ti produced by selective laser melting in HCl solution. *J. Alloys Compd.* **2020**, *820*, 153422. [[CrossRef](#)]
38. Zhao, P.C.; Yuan, G.J.; Wang, R.Z.; Guan, B.; Jia, Y.F.; Zhang, X.C.; Tu, S.T. Grain-refining and strengthening mechanisms of bulk ultrafine grained CP-Ti processed by L-ECAP and MDF. *J. Mater. Sci. Technol.* **2021**, *83*, 196–207. [[CrossRef](#)]
39. Su, B.X.; Luo, L.S.; Wang, B.B.; Su, Y.Q.; Wang, L.; Ritchie, R.O.; Guo, E.Y.; Li, T.; Yang, H.M.; Huang, H.G.; et al. Annealed microstructure dependent corrosion behavior of Ti-6Al-3Nb-2Zr-1Mo alloy. *J. Mater. Sci. Technol.* **2021**, *62*, 234–248. [[CrossRef](#)]
40. Chiu, T.M.; Mahmoudi, M.; Dai, W.; Elwany, A.; Liang, H.; Castaneda, H. Corrosion assessment of Ti-6Al-4V fabricated using laser powder-bed fusion additive manufacturing. *Electrochim. Acta* **2018**, *279*, 143–151. [[CrossRef](#)]
41. Qiao, Y.X.; Wang, X.Y.; Yang, L.L.; Wang, X.J.; Chen, J.; Wang, Z.B.; Zhuo, H.L.; Zou, J.S.; Wang, F.H. Effect of aging treatment on microstructure and corrosion behavior of a Fe-18Cr-15Mn-0.66N stainless steel. *J. Mater. Sci. Technol.* **2022**, *107*, 197–206. [[CrossRef](#)]
42. Zheng, Z.B.; Long, J.; Guo, Y.; Li, H.; Zheng, K.H.; Qiao, Y.X. Corrosion and impact-abrasion-corrosion behaviors of quenching-tempering martensitic Fe-Cr alloy steels. *J. Iron Steel Res. Int.* **2022**, *29*, 1853–1863. [[CrossRef](#)]
43. Balyanov, A.; Kutnyakova, J.; Amirkhanova, N.A.; Stolyarov, V.V.; Valiev, R.Z.; Liao, X.Z.; Liao, X.Z.; Zhao, Y.H.; Jiang, Y.B.; Xu, H.F.; et al. Corrosion resistance of ultra fine-grained Ti. *Scr. Mater.* **2004**, *51*, 225–229. [[CrossRef](#)]
44. Saadi, S.A.; Yi, Y.S.; Cho, P.; Jang, C.H.; Beeley, P. Passivity breakdown of 316L stainless steel during potentiodynamic polarization in NaCl solution. *Corros. Sci.* **2016**, *111*, 720–727. [[CrossRef](#)]
45. Kim, H.S.; Kim, W.J. Annealing effects on the corrosion resistance of ultrafine-grained pure titanium. *Corros. Sci.* **2014**, *89*, 331–337. [[CrossRef](#)]
46. Gu, Y.X.; Jiang, J.H.; Ma, A.B.; Lu, L.H.; Wu, H.R. Corrosion behavior of pure titanium processed by rotary-die ECAP. *J. Mater. Res. Technol.* **2021**, *15*, 1873–1880. [[CrossRef](#)]
47. Liu, L.; Liu, Y.; Wang, F.H. Electrochemical Corrosion Behavior of Nanocrystalline Materials—a Review. *J. Mater. Sci. Technol.* **2010**, *26*, 1–14. [[CrossRef](#)]
48. Chi, G.F.; Yi, D.Q.; Liu, H.Q. Effect of roughness on electrochemical and pitting corrosion of Ti-6Al-4V alloy in 12 wt.% HCl solution at 35 °C. *J. Mater. Res. Technol.* **2020**, *9*, 1162–1174. [[CrossRef](#)]
49. Li, W.; Li, D.Y. Influence of surface morphology on corrosion and electronic behavior. *Acta Mater.* **2006**, *54*, 445–452. [[CrossRef](#)]

- 
50. Zhang, X.; Wu, G.; Peng, X.; Li, L.; Feng, H.; Gao, B.; Huo, K.; Chu, P.K. Mitigation of corrosion on magnesium alloy by pre-designed surface corrosion. *Sci. Rep.* **2015**, *5*, 17399. [[CrossRef](#)]
  51. Wu, H.; Shi, Z.; Zhang, X.; Qasim, A.M.; Xiao, S.; Zhang, F.; Wu, Z.; Wu, G.; Ding, K.; Chu, P.K. Achieving an acid resistant surface on magnesium alloy via bio-inspired design. *Appl. Surf. Sci.* **2019**, *478*, 150–161. [[CrossRef](#)]